THE IMPACT OF MEMBRANE CONSTRAINT ON PEM FUEL CELL WATER MANAGEMENT

IGOR NAZAROV* AND KEITH PROMISLOW†

Abstract. A non-equilibrium force-balance model for water transport within a Nafion type polymer electrolyte membrane fuel cell is developed. The model combines earlier work of Choi *et. al.*, which describes the Schroeder paradox in terms of a capillary pressure jump, with a pressure based description of water transport including the partitioning of external pressure between the polymer backbone and the liquid water. The model addresses the impact of mechanical compression upon water and ion transport, and identifies operating conditions in which a liquid water equilibrated cathode can co-exist with a vapor equilibrated anode. The model predicts that mechanical compression will decrease membrane water content by 5-30%, and decreases back-diffusion of water within the membrane by up to 20%.

Key words. Mechanical constraint, PEM fuel cell, Water Management, Schroeder paradox

1. Introduction. Polymer electrolyte membrane (PEM) fuel cells are low-temperature systems which efficiently convert chemical energy to electromotive force at power densities commensurate with the needs of automotive applications. The Nafion membrane which forms the heart of PEM fuel cells must be hydrated to be an effective proton conductor. A key issue in the operation of PEM fuel cells is water management: maintaining membrane hydration while avoiding excessive water accumulation in catalyst layers which limits gas, particularly oxygen, transportation. A central role in water balance is played by the so-called Schroeder paradox, [12, 17, 18]: the water sorption isotherms of Nafion equilibrated with saturated vapor does not match the liquid water equilibrated isotherms, and moreover jump in membrane equilibrium water content between liquid and saturated vapor equilibration grows with increasing temperature [4].

Recently Choi *et. al.* [2], have proposed an equilibrium model which models the Schroeder paradox in terms of capillary pressure, the presence of liquid water removes the meniscus present at the hydrophilic pores of the membrane. In their approach the water sorption isotherms are replaced with a balance between water activity and liquid water pressure within the membrane. They also introduce isotherms for the component of membrane water which is chemisorpted, and hence less mobile. This force-balance modeling for the Schroeder paradox opens the way for a *non-equilibrium* force-balance model which can incorporate mechanical constraints in a self-consistent manner. Such a model can attempt to incorporate membrane compression and to address a major limitation of water management models to date: the lack of a self-consistent model which can accommodate a liquid equilibrated cathode and a vapor equilibrated anode under typical PEM fuel cell operating conditions.

While direct experimental methods to observe PEM fuel cells lack detailed resolution within the membrane electrode assembly (MEA), the available experimental evidence indicates that a saturated cathode gas channel, with liquid water in the cathode electrode, and a saturated or nearly saturated anode channel, without liquid water in the anode electrode, is a typical operational condition for the majority of the active area of a unit cell. The combination of a liquid equilibrated cathode side of the membrane with a vapor equilibrated anode, and a strong Schroeder effect at 80° C, generates a significant gradient of water concentration across the membrane. Models which employ experimentally measured water self-diffusivities, or water permeabilities, predict a substantial flux of water from cathode to anode under these liquid/saturated vapor equilibrium conditions, a flux greater than the osmotic drag from anode to cathode. Moreover with a saturated anode gas channel, the only mechanism to remove vapor from the anode electrode is the temperature gradient from membrane to channel which induces a gradient in the temperature dependent vapor saturation. If the cathode to anode water flux exceeds the osmotic flux by an amount greater than the maximal vapor flux the anode electrode can accommodate, then there is no self-consistent "dry anode" regime.

Several attempts have been made to accommodate this behavior. Most notably the models of Weber and Newman, [14, 15], which propose a degenerate transport mechanism for the membrane. Namely, at high liquid pressure the water transport is driven both by pressure and diffusion, however below a critical liquid pressure the pores of the membrane close, and transport becomes diffusive only. This degenerate diffusion permits large water gradients without large water fluxes, however

*Dept. of Mathematics, Michigan State University, East Lansing, USA (kpromisl@math.msu.edu)
†Dept. of Mathematics, Michigan State University, East Lansing, USA (kpromisl@math.msu.edu).

it is based upon a speculative thermodynamic reorientation of the membrane. Moreover at typical operating conditions, for example 3 Atms pressure on the cathode side, the model predicts the entire membrane will be in the pressure driven transport phase with a large membrane water flux incompatible with a vapor equilibrated anode electrode.

The model presented here exploits Choi's capillary pressure model for membrane equilibrium, using it to provide boundary conditions for a pressure driven flow model. A key feature of the model is the coupling of the membrane water uptake to the elastic constraints imposed by the MEA and flow fields. As the membrane absorbs water it must expand, compressing the MEA. This leads to a competition, through the force balance, with the capillary pressure. This coupling disproportionately lowers the water sorption isotherms at the wetter cathode end of the membrane, reducing the transport of water from cathode to anode.

2. Model Presentation. We propose that at equilibrium the membrane water uptake of Nafion is dictated by a balance between internal osmotic pressure of the solvent waters within the pores and the elastic forces of the polymer matrix which depend in turn on temperature and pretreatment, [5]. Recent interpretations of SAX data of Nafion, [11], indicate a phase separation into long cylindrical agglomerates of PTFE, roughly 4 nanometers in diameter and 100 nanometers in length surrounded by solvent waters. This micro-structure depends upon pretreatment of which there are three standard forms. In the expanded form (E) the membrane is boiled in 3% H_2O_2 solution followed by boiling in 0.5 molar H_2SO_4 to ensure full protonation, and finally in deionized water. The membrane can also be dried at 80°C to produce the normal form (N), or dried at 105°C to produce the shrunk form (S). The model contains four parameters which account for the various possible micro-structures, K_b, an effective bulk modulus for dilational strain, K_s, a modulus for lateral compression of the polymer agglomerates which serves to transfer the compressional strain to the water, V_{w0}, the reference volume of the hydrophilic domain within a reference volume V_0, and V_{s0}, the reference volume of polymer agglomerates within the unstressed (and unswollen) material.

We consider a 1D section of membrane exposed to gas at a prescribed relative humidity on the anode side, and to either gas or liquid water on the cathode side. A prescribed current is driven thought the membrane, which is assumed to expand uniaxially into the surrounding gas diffusion layer (GDL) in response to water uptake. We denote by $c_a = [SO_3^-]$ and $c_w = [H_2O]$ the local molar concentration of the acid groups and water in the membrane. The acid concentration varies with the water uptake, from the dry acid group concentration, a_0, in the unswollen membrane to a more dilute form in the hydrated membrane. We nondimensionalize the water concentration by the swelling dependent acid group concentration, so that $C_w = c_w/c_a$ represents the dimensionless water concentration per acid group.

Membrane Isotherms. In [2] Choi *et. al.* capture the membrane water equilibrium isotherms as a balance between water activity outside the membrane, a_{out}, against water activity, a_w, and water pressure, P_w, inside the membrane. A key component in the osmotic pressure is the capillary pressure, P_c, which, following the Laplace-Young equation, depends upon the liquid-membrane contact angle. The equilibrium with the environment is described by the following equation

$$\ln \frac{a_w}{a_{\text{out}}} + \frac{\bar{V}}{RT}(P_w + P_c) = 0. \tag{2.1}$$

The capillary pressure is positive to reflect the hydrophilicity of the channels inside the membrane. The pressure gradient is directed outwards, which correlates with the inequality $a_w < a_{\text{out}}$ for fixed C_w. Within this context the Schroeder paradox arises via the jump in liquid pressure which occurs when the hydrophilic meniscus is removed (that is, P_c is set to zero).

A key modeling issue is the dependence of the capillary and water pressure on temperature. The data collected by Hinatsu *et. al.* [4], show that the jump in equilibrium water content of Nafion 117 from the saturated vapor to liquid equilibrated state is relatively small at $T = 30°C$ but more significant at $T = 80°C$ (see Figure 2). With the context of Choi *et. al.*'s force balance relation (2.1) this can be explained only if the capillary pressure is made to increase with temperature. Moreover, independent of the Schroeder paradox jump, Hinatsu *et. al.* observed that the equilibrium water content in the liquid equilibrated membrane increases with temperature as is consistent with a membrane which softens with increasing temperature, decreasing the liquid pressure, P_w, and permitting more water uptake.

Chemisorpted and Physiosorpted waters. Choi *et. al.* also describe the sorption of water within the membrane. The waters of hydration surrounding the dissociated acid groups within the membrane, the chemisorpted water, have restricted mobility. On the other hand, they serve to shield the electric forces, allowing protonic defects and non-chemisorbed waters enhanced freedom of motion within the center of the pores. The water molecules are thus classified into two categories, those bound to the acid groups, chemisorption – C_w^c, and free molecules, physiosorption – C_w^f. The total water concentration is merely the sum of the two $C_w = C_w^c + C_w^f$. Choi *et. al.* relate the concentration of chemisorpted water at equilibrium to the activity of free water via the relation

$$a_w = \frac{C_w^f}{1 + C_w^f}. \tag{2.2}$$

Using a standard chemical equilibrium relating reactant concentrations to the Gibbs exchange energy, and assuming the first hydration shell is the most strongly bound, Choi *et. al.* derive an expression for the local water concentration (per acid group) in terms of C_w^f and a_w

$$C_w = C_w^f \left(\lambda K_1 \frac{1 + (-(1+\nu) + \nu a_w) a_w^\nu}{1 + (K_1 - 1 - K_1 a_w^\nu) a_w} + 1 \right). \tag{2.3}$$

Here K_1 is the equilibrium constant for the first hydration shell and ν is the number of waters participating in the hydration shell. The hydronium concentration is taken at equilibrium with water,

$$C_+ = -\frac{1}{2} K_{eq} C_w + \sqrt{\left(\frac{1}{2} K_{eq} C_w \right)^2 + K_{eq} C_w}. \tag{2.4}$$

Stress-strain relationship. We assume uniaxial deformation of the membrane with water uptake. The external pressure acting upon the membrane is partitioned between the water network, which occupies the hydrophilic pores, and the back-bone structure of the cross-linked membrane, see Figure 1 (Left). The elastic deformation of the media is described by K_b, the modulus for dilatational deformation, and K_s, a modulus for lateral compression of the elongated polymer aggregates. The water pushes laterally on the polymer aggregates, which couples to the dilatometric strain in the backbone structure,

$$\varepsilon_b = \frac{V - V_0}{V_0} \tag{2.5}$$

where $V_0 = V_{w0} + V_{s0}$ is the reference volume and $V = V_s + V_w$ is characteristic volume after deformation. Liquid water is incompressible, with its local volume given by

$$V_w = a_0 \bar{V} V_0 = a_0 C_w \bar{V} V_0, \tag{2.6}$$

where $\bar{V}$ is the partial molar volume of water. Dilatometric expansion of the water filled pores and corresponding strain in the polymer aggregates are denoted by

$$\varepsilon_w = \frac{V_w - V_{w0}}{V_{w0}}, \tag{2.7}$$

$$\varepsilon_s = \frac{V_s - V_{s0}}{V_{s0}}. \tag{2.8}$$

From the shared force balance depicted in Figure 1 the strain in the backbone can be written as

$$\varepsilon_b = \frac{V_{w0}\varepsilon_w + V_{s0}\varepsilon_s}{V_{w0} + V_{s0}}. \tag{2.9}$$

Combining equations (2.7-2.6), yields

$$\varepsilon_b = \alpha C_w + \beta \varepsilon_s - (1 - \beta), \tag{2.10}$$

where the nondimensional parameter $\alpha = a_0 \bar{V}$ connects C_w with the strain. The reference volumes enter into the model only through the dimensionless volume fractions $\beta = V_{s0}/V_0$ and $1-\beta = V_{w0}/V_0$. The average pore radius is defined as the cube root of the local water volume which takes the form

$$r_p \equiv \sqrt[3]{V_w} = r_p \sqrt[3]{\alpha C_w}. \tag{2.11}$$

The force balance in the membrane equates the total external pressure to the sum of the stress born by the backbone and the hydrophilic domains of the membrane,

$$K_s\varepsilon_s + K_b\varepsilon_b + P_e = 0. \tag{2.12}$$

From the equations (2.10-2.12) we obtain expressions for the lateral strains of the polymer agglomerates and the dilitational strain of the backbone in terms of the local water uptake and external pressure,

$$\varepsilon_s = -\frac{K_b(\alpha C_w - (1-\beta)) + P_e}{K_s + \beta K_b}, \tag{2.13}$$

$$\varepsilon_b = \frac{K_s(\alpha C_w - (1-\beta)) - \beta P_e}{K_s + \beta K_b}. \tag{2.14}$$

Due to the swelling of the membrane the through-plane Lagrangian and Eulerian coordinates, z and z', are related by

$$dz' = (1 + \varepsilon_b(z))dz. \tag{2.15}$$

In particular the dimensional acid concentration dilutes with the swelling, $c_a = a_0/(1+\varepsilon_b)$. From the incompressibility of the liquid water, the total water uptake per unit area is related to the strain via

$$\bar{c}_w = \int_0^{L'} c_w(z')dz' = \int_0^{L'} c_a(z')C_w(z')dz' = a_0\int_0^{L} C_w(z)dz, \tag{2.16}$$

where L is the width of unstrained membrane and $(L'-L)/L$ is the total swelling percentage.

The liquid pressure balances with the lateral pressure in the agglomerates,

$$P_w = -K_s\varepsilon_s(C_w, P_e), \tag{2.17}$$

see Figure 1 (Left). The membrane is clamped between two elastic gas diffusion layers with bulk moduli K_e and unconstrained thickness L_e, see Figure 1 (Right). The swelling of the membrane into the GDL generates the external pressure which constrains the membrane, this results in a nonlocal equation relating the external pressure to the swelling,

$$P_e = \frac{K_e}{L_e}\int_0^L \varepsilon_b(C_w(z), P_e)dz. \tag{2.18}$$

Water and Proton flux. We employ the assumption, used in [1] and [9], in which the hydrogen reduction reaction is followed by hydronium formation, so that at the anode we have the reaction

$$H_2 + 2H_2O \rightarrow_{\mathrm{Pt}} 2H_3O^+ + 2e^-,$$

while at the cathode the oxygen reduction reaction takes the form

$$O_2 + 4H_3O^+ + 4e^- \rightarrow_{\mathrm{Pt}} 6H_2O.$$

In particular our model assumes the protons are transported across the membrane as hydronium. Fluxes of water and hydronium through the membrane are given by the Nernst-Planck equations

$$J_w = -\kappa_w(C_w^f)a_0C_w^f(\partial_z P_w + a_0\chi(C_w^f)FC_+\partial_z\phi) - D_w a_0\partial_z a_w, \tag{2.19}$$

$$J_+ = -D_+a_0\partial_z C_+ - D_+a_0\frac{F}{RT}C_+\partial_z\phi + W_+C_+J_w, \tag{2.20}$$

where ϕ denotes the electric potential. From the experimental data of Meier and Eigenberger, [8], we fit the membrane permeability, κ_w, as a function of water content and the water drag coefficient, χ, as given in Table 1. The water drag coefficient takes a value of 2 waters/proton at $C_w = 13$, with a limiting value of 3 waters/proton achieved for $C_w > 22$. In a pressure driven model for water transport the water self-diffusivity plays a minor role and is taken constant. The hydronium

diffusivity D_+ largely dictates the membrane conductivity and depends upon water content, see Table 1. Conservation of mass at the anode and cathode catalyst layers, and the relation $J_+ = -I/F$, result in the boundary conditions

$$-J_w + \frac{3I}{2F} = N_w^c, \tag{2.21}$$

$$J_w - \frac{I}{F} = N_w^a. \tag{2.22}$$

Based on the equilibrium relation (2.1) the net exchange of water with the GDL is taken to be linearly proportional to the disequilibrium between the membrane and its environment,

$$N_w^c = \gamma \left(\ln \frac{a_w^c}{a_v^c} + \frac{\bar{V}}{RT}(P_w + P_c) \right), \tag{2.23}$$

$$N_w^a = \gamma \left(\ln \frac{a_w^a}{a_v^a} + \frac{\bar{V}}{RT}(P_w + P_c) \right), \tag{2.24}$$

with positive fluxes out of the membrane. The water exchange parameter γ models the rate limitations implicit in water sorption from the membrane. A study of the impact of this parameter on fuel cell models was considered in detail in Ge *et. al.* [3], where different values were taken for adsorption and desorption. We take a single value of γ for both processes, but following Ge let γ increase with water content,

$$\gamma = \gamma_0 \left(0.5 \tanh \left(\frac{C_w - 12}{5} \right) + 1.5 \right). \tag{2.25}$$

The capillary pressure relates to the liquid-membrane contact angle, θ, through the Laplace-Young equation

$$P_c = -\frac{2\sigma \cos\theta}{r_p}, \tag{2.26}$$

where r_p is the average pore radius. To fit the dependency of the Schroeder jump on temperature observed in Hinsatu *et. al.* [4], we adjust the contact angle θ to vary linearly with temperature, from 91° at $T = 30^\circ$C to 126° at $T = 80^\circ$C.

Cell Voltage. The cell voltage is determined from the voltage balance equation

$$V = E_0 - \eta - \Delta\phi, \tag{2.27}$$

where E_0 is the open circuit potential, η, is the cathode overpotential given by the Butler-Volmer equation in terms of the prescribed current density and oxygen concentration

$$I = i_*(C_o - \delta I) \left(\exp\left[\frac{\alpha F}{RT}\eta \right] - \exp\left[-\frac{\alpha F}{RT}\eta \right] \right), \tag{2.28}$$

and δ is a mass transport parameter for oxygen in the catalyst layer. The voltage loss in the membrane, $\Delta\phi \equiv \phi(\text{anode}) - \phi(\text{cathode})$, is calculated from the hydronium flux equation (2.20).

3. Results and Discussion. We compare the model predictions to available data. The model is computed in a 1D setting, calculating through plane water profiles, stress, swelling, and effective bulk parameters such as protonic resistivity. The 1D setting corresponds to a membrane exposed to an environment which is uniform in-plane. We model only the membrane, treating the gas diffusion and catalyst layers within the boundary conditions through effective transport parameters. The current density and ambient environment of the membrane, including relative humidity and presence of liquid water, are taken as control parameters.

The force balance model predicts the water uptake isotherms as a function of the elastic moduli of the membrane, the chemio- and physiosorpted water contents, and on the capillary pressure. The model cannot predict the transitions between the S, N, and E forms of Nafion. These correspond to different microstructural arrangements of the polymer agglomerates, and hence to different elastic moduli and reference volume fractions. The internal elastic moduli and volume fractions are fit

to the N-form data of Hinsatsu *et. al.*. The agreement between their measured isotherms and the computed ones are presented in Figure 2 at 30° and 80°C. The fit to the liquid equilibrated isotherms measured by Hinsatu *et. al.* [4] was made by taking K_b and K_s, the moduli of dilatational and lateral compression, to be equal, $K_s = K_b = K(T)$, where $K(T)$ decreases with temperature in the form

$$K(T) = \left[9 - 4.75\frac{(T - 303.16)}{50}\right] \times 10^7. \tag{3.1}$$

This is a 20% varition from experimental data, see Figure 5 of [7]. In particular the bulk moduli decreases from 90 to 42.5 MPa as the temperature ranges from 30° to 80°C. The reference volume fractions $\beta = V_{s0}/V_0 = 0.95$.

The jump from the vapor isotherms at saturation (external RH=1) to the liquid isotherms are a measure of the capillary pressure P_c, which is made temperature sensitive through the contact angle $\theta = \theta(T)$. The choices of $K(T)$ and $\theta(T)$, together with the chemisorption isotherms (2.3), fix the vapor isotherms as a function of external RH. Their qualitatively good fit to the data is obtained without further adjustment of parameters. The difference between the the vapor isotherms at the two temperatures arises primarily from the softening of the backbone material with higher temperature. The lower elastic moduli decreases the water pressure which through (2.23-2.24) increase the membrane water activity, and hence the water content through the activity relation (2.2). The inset of Figure 2 shows the isotherms for a liquid water equilibrated membrane. The difference between saturated vapor and liquid equilibration is explained by the removal of the capillary pressure. As the pores are hydrophilic this leads to a decrease in liquid water pressure and a corresponding jump in water adsorption. Hinsatsu's liquid equilibrated isotherms were used to determine the liquid-pore wall contact angle, as a function of temperature, giving the observed fit to the data.

The impact of mechanical constraint on the isotherms is also depicted in Figure 2, where the vapor and liquid isotherms of the constrained membrane are displayed as dotted lines. Compared to the unconstrained case, the water content of the constrained membrane falls by 5-20% under vapor equilibrated, with the largest percentage decrease coming at the highest water contents. Under liquid equilibration the isotherm falls by almost 30%, from roughly 22 to 16 waters/acid group at 80°. This disproportionate decrease has the effect of reducing the impact of the Schroeder paradox, particularly at higher temperatures, by reducing the cathode to anode water gradient under liquid/saturated vapor conditions.

The presence of current impacts the water profile since it generates water, and pulls water from the anode to the cathode via the electro-osmotic drag. In Figure 3 the solid curves depict the membrane swelling as a function of the external modulus of the GDL material at a current density of 1 A/cm^2 at two temperatures with a liquid equilibrated cathode and a saturated vapor equilibrated anode. The hotter membrane is wetter, and more swollen, at low external constraint, due to the softer elastic moduli and greater water uptake. However at larger external moduli the softer membrane material is less resistance to the external compression and it is the colder membrane which has the larger swelling. At both temperatures the membrane is essentially fully constrained at an external moduli between 10^8 and 10^9 Pascals. The dotted curves shows the pressure exerted on the membrane verses the elastic modulus of the GDL. This curve saturates at large external moduli since the swelling pressure generated by the membrane is limited by membrane's ability to absorb liquid.

The water profile through the membrane is linear to good approximation. In Figure 4 the water contents at the anode and cathode ends of the membrane are shown as a function of current density for both constrained and unconstrained operation, for both saturated vapor anode/cathode boundary conditions and liquid equilibrated cathode/saturated vapor anode boundary conditions. In all cases the anode water content falls with increasing current density, while the cathode rises, a reflection of the increasing water drag. Under constraint the cathode water content falls significantly more than the anode, reducing the water content gradient, this is particularly true when the cathode is liquid equilibrated. Figure 5 presents the average membrane water content of a liquid equilibrated cathode/saturated vapor equilibrated anode as a function of current density at both 30° and 80°C and for high (1.2) and low (0.7) values of the water exchange coefficient, γ. Because of the high cathode water content at 80°C for liquid equilibration, the average water content is always higher at 80°C than at 30°C, despite the vapor isotherms being higher at the lower temperature. Moreover the high water content on the cathode and low anode content at 80°C leads to less net swelling as compared to 30°C, as shown in Figure 3, despite the higher average water content.

Figure 6 shows the impact of constraint on both the average water content and a scaled water content gradient as a function of current density for constrained and unconstrained membranes and as a function of external elastic modulus for two different values of the water exchange coefficient γ. In Figure 6 (Left), consistent with previous observations, the constrained membrane has both lower water content and a lower water gradient. The water content gradient increases in magnitude with current density, but decreases in magnitude with constraint. This is a key observation, the constraint serves to decrease the water content gradient, reducing back diffusion. In Figure 6 (Right), we see the constraint begins to have impact at $\kappa_e = 10^7$ Pa, and the membrane is essentially fully constrained at $\kappa_e = 10^8$ Pa.

In Figure 7 (Left) the dependence of ohmic losses is shown as a function of current density for the constrained and unconstrained cases with a wet cathode and a saturated vapor equilibrated anode at two temperatures. At 80°, the large water gradient present across the membrane induces significant water flux, whose drag on the current produces a voltage drop which is independent of the current. Thus the ohmic losses, defined as ϕ(cathode)-ϕ(anode), does not approach zero at zero current density for these boundary conditions. At 30° C this effect is much smaller. In Figure 7 (Right) the membrane resistence is shown for homogenious boundary conditions (saturated vapor at both anode/cathode or liquid at both anode/cathode) for different current densities. The impact of constraint on the membrane resistence is secondary to the switch from saturated vapor to liquid equilibration at 80°.

In Figure 8 the dependence of the membrane resistance upon constraint is compared with experimental data from [16]. Both the computational and the experimental data are for liquid anode/cathode equilibration. The experimental data is taken at 30°C, and both sets show a 10% increase in membrane resistence with compression. The hysteresis present in the experimental data is accounted for in the model, moreover the difference in magnitude of resistivity could arise from the fact that the experiments are conducted on recast Nafion 115, and that contact resistence present in the experimental data is not reflected in the model.

Anode Wetting. A difficult issue in the modeling of water transport in PEM fuel cells is to self-consistently determine the status of water in the anode catalyst layer when the cathode is wet. At 80°C, the Schroeder jump in liquid water at the cathode generates a water concentration gradient within the membrane which, for the experimentally measured water self-diffusivities/permiabilities, would ignite back diffusion sufficient to flood the anode side of the membrane.

To address the impact of membrane compression on water transport and anode wetting, we consider a typical regime in which the cathode is two-phase and the anode is exposed to almost saturated vapor. Neglecting convective transport, previous analysis, [10], has shown that the maximal vapor flux which can be carried by the anode GDL filled with almost saturated vapor is determined by the temperature gradient and the saturation profile,

$$N_v^{\max} = -D_v \partial_z C_{sat} = -D_v C'_{sat}(T) \partial_z T. \tag{3.2}$$

The gradient of the temperature is proportional to the heat production, which at steady-state leaves roughly half through the anode and half through the cathode, so that

$$-\kappa_h \partial_z T = \frac{1}{2} \Delta V \cdot I, \tag{3.3}$$

where the voltage loss ΔV is defined as the difference between the reference voltage and the cell voltage. From (2.27), replacing the voltage drop with its ohmic equivalent, the voltage loss takes the form

$$\Delta\phi = E_{\text{ref}} - (E_0 - I/\sigma - \eta(C_o, I)). \tag{3.4}$$

The maximal vapor flux which can be carried by the anode in a dry regime is

$$N_v^{\max} = \frac{D_v}{2\kappa_h} C'_{sat}(T) F E_{\text{ref}} \cdot \frac{\Delta V}{E_{\text{ref}}} \frac{I}{F}. \tag{3.5}$$

The percent voltage loss $\Delta V / E_{\text{ref}}$ varies from about 25% at low current to about 50% at current current density of 1 Amp/m^2.

Figure 9 depicts the fluxes as a function of current density for constrained and unconstrained operation and the state of the anode electrode as a function of the GDL modulus at a current density

of 1 Amp/cm^2. In Figure 9 (Left) the maximal vapor flux which can be carried by the anode, $N_v^{\max}$, is plotted together with the computed vapor flux into the anode, N_w^a, for a liquid equilibrated cathode and a saturated vapor equilibrated anode. While $N_v^{\max}$ increases with current density, N_w^a decreases due to the electro-osmotic drag. The critical current density at which the two curves intersect is denoted by I^*, the *minimal* current at which the anode will remain dry if the cathode is held wet. The effect of constraint is significant, since it reduces the water gradient through the membrane and hence reduces back diffusion, lowering N_w^a and I^*. Figure 9 (Right) shows I^* as a function of the external pressure, decreases from roughly 0.98 A/cm^2 for an unconstrained membrane to 0.78 A/cm^2 for a fully constrained membrane. The rough nature of the estimate of $N_v^{\max}$ makes the calculation of I^* approximate, however it is clear that the 20% decrease in water cross-over due to constraint has a significant impact on water management.

REFERENCES

[1] P. Berg, K. Promislow, J. St. Pierre, J. Stumper, B. Wetton, Water management in PEM fuel cells, *J. Electrochem. Soc.* **151** (No. 3) (2004) A341-A354.

[2] P. Choi, N.H. Jalani, and R. Datta. Thermodynamics and proton transport in Nafion. I. Membrane swelling, sorption, and ion-exchange equilibrium. *J. of Electrochem. Soc.*, Vol. 152(3), E83-E89, 2005.

[3] S. Ge, X. Li, B. Yi, I-M. Hsing, Absorption, desorption, and transport of water in polymer electrolyte membrane fuel cells, *J. Electrochem. Soc.* **152** (6) A1149-1157, (2005).

[4] J.T. Hinatsu, M. Mizuhata, and H. Takenaka. Water uptake of perfluorosulphonic acid membranes from liquid water and water vapor. *J. Electrochem. Soc.* Vol 141, No. 6, 1493–1498, 1994.

[5] W.Y. Hsu and T.D. Gierke, Ion clustering and transport in Nafion Perfluorinated membranes, *Macromolecules* **15** 101 (1982).

[6] J.Y. Huh, and Y.C. Bae. Water activities of florinated solid polymer electrolyte/water systems using group–contribution method. *Chemical Engineering Science*, Vol. 57, 2747–2752, 2002.

[7] Lai, Y.-H., C. Mittelsteadt, C. Gittleman, D. Dillard, Viscoelastic stress model and mechanical characterization of perfluorosulfonic acide (PFSA) polymer electrolyte membranes, *Proc. FUELCELL2005*, Third International Conf. on Fuel Cell Science, May 23-25, 2005, Ypsilanti Michigan.

[8] F. Meier and G. Eigneberger, Transport paramters for the modelling of water transport in ionomer membranes for PEM-fuel cells, *Electrochimica Acta* **49** 1731-1742 (2004).

[9] I. Nazarov and K. Promislow, Ignition Bifurcations in a Stirred Tank PEM Fuel Cell, *Chemical Engineering Science* **61** (10) (2006) 3198-3209.

[10] K. Promislow, J. Stockie, B. Wetton, A sharp interface reduction for for multiphase flow in a porous PEM fuel cell electrode, *Proc. Roy. Soc. London: Series A* **462** No. 2067 (2006) 241-261.

[11] L. Rubatat, A.L. Rollet, G. Gebel, O. Diat, Evidence of elongated polymer aggregates in Nafion, *Macromolecules* **35** 4050-4055, (2002).

[12] P. Schroeder, *Z. Phys. Chem.* **45** (75) (1903).

[13] M.B. Satterfield, P. W. Majsztik, H. Ota, J. Benziger, A. Bocarsly, Mechanical properties of Nafion and Titania/Nafion composite membranes for polymer electrolyte membrane fuel cells, *J. Polymer Science Part B: Polymer Physics*, **44** 2327-2345 (2006).

[14] A. Weber and J. Newman, Transport in polymer-electrolyte membranes III: Model validation in a simple fuel-cell model, *J. Electrochem. Soc.* **151** (2) A316-339 (2004).

[15] A. Weber and J. Newman, A theoretical study of membrane constraint in polymer-electrolyte fuel cells, *AIChE* **50** (12) 3215-3226.

[16] C. Yang, S. Srinivasan, A.B. Bocarsly, S. Tulyani, and J.B. Benziger. A comparison of physical properties and fuel cell performance of Nafion and Zirconium phosphate/nafion composite membranes. 2003.

[17] T. Zawodzinski, C. Derouin, S. Radzinksi, R. Sherman, V. Smith, T.E. Springer, and S. Gottesfeld, *J. Electrochem. Soc.* **140** 1041 (1993).

[18] T. Zawodzinski, T.E. Springer, J. Davey, R. Jestel, C. Lopez, J. Valerio, and S. Gottesfeld, *J. Electrochem. Soc.* **140** 1981 (1993).

a_0	1200	dry acid molar concentration	mol/ m^3
D_v	$8 \cdot 10^{-6}$	vapor diffusivity in GDL	m^2/s
D_w	10^{-8}	water diffusivity in membrane	m^2/s
$D_+(C_w)$	$10^{-8}\frac{C_w}{20}$	proton diffusivity in membrane	m^2/s
E_{ref}	1.2	Reference reaction voltage	V
I	0-1.5	current density	$Amp/(m^2s)$
K_{ext}	10^9	bulk modulus of gas diffusion layer	Pa
K_1	100	equil. constant for first hydration shell	-
L	$2.5 \cdot 10^{-5}$	width of membrane	m
L_e	10^{-5}	width of GDL	m
P_c	(2.26)	capillary pressure	Pa
r_p	$5 \cdot 10^{-9}$	typical pore radius within membrane	m
R	8.31	Universal gas constant	J/(mol ° K)
T	303-353	temperature	°K
$\bar{V}$	$1.8 \cdot 10^{-5}$	water partial volume	m^3/mol
β	0.95	Ref. volume fraction of polymer	-
γ	1.2	water exchange coefficient with GDL	$mol/(m^2s)$
$\eta_w(T)$	0.0436/(T+297)	dynamic viscosity of water	Pa s
κ_h	0.5	Electrode thermal conductivity	J/(m s °K)
$\kappa_p(C_w)$	$(.4 + .074 \cdot C_w^2) \cdot 10^{-20}$	membrane water permeability	m^2
$\kappa_w(C_w, T)$	κ_p/η_w	Darcy's coefficient	$m^5/(J\ s)$
$\mu_+(C_w)$	$D_+/(RT)$	proton mobility	m^2 mol/(J s)
σ	$7.21 \cdot 10^{-2}$	water surface tension	J/m^2
χ	$2 + \tanh((C_w - 13)/5)$	water drag coefficient	-

Table 1: Dimensional Parameters

	$T = 30°$ C	$T = 80°$ C	
K_b	$9.0{\cdot}10^7$ Pa	$4.25{\cdot}10^7$ Pa	effective bulk modulus of polymer backbone
K_s	$9.0{\cdot}10^7$ Pa	$4.25{\cdot}10^7$ Pa	effective bulk modulus of side chains
θ	$91°$	$126°$	contact angle for water with hydrophobic backbone
λ	1.6	1.7	monolayer coverage being bound
ν	5	6	number of water participating in hydration shell

Table 2: Temperature dependent parameters

	units	
$a_{\text{in/out}}$	-	water activity in/outside of membrane
a_w	-	water activity inside membrane
c_a	mol/m^3	Acid group molar concentration
C_w	mol/m^3	Total membrane water concentration
C_w^f	mol/m^3	Free membrane water concentration
C_+	mol/m^3	Membrane hydronium concentration
J_w	mol/(m^2 s)	Water flux through membrane
J_+	mol/(m^2 s)	hydronium flux through membane
$N_w^{a/c}$	mol/(m^2 s)	water flux into anode/cathode electrode
P_e	Pa	external pressure compressing membrane
P_w	Pa	water pressure
$\epsilon_{b,s,w}$	-	strain of backbone/sidechain/water
ϕ	V	electric potential within membrane

Table 3: Dimensional variables

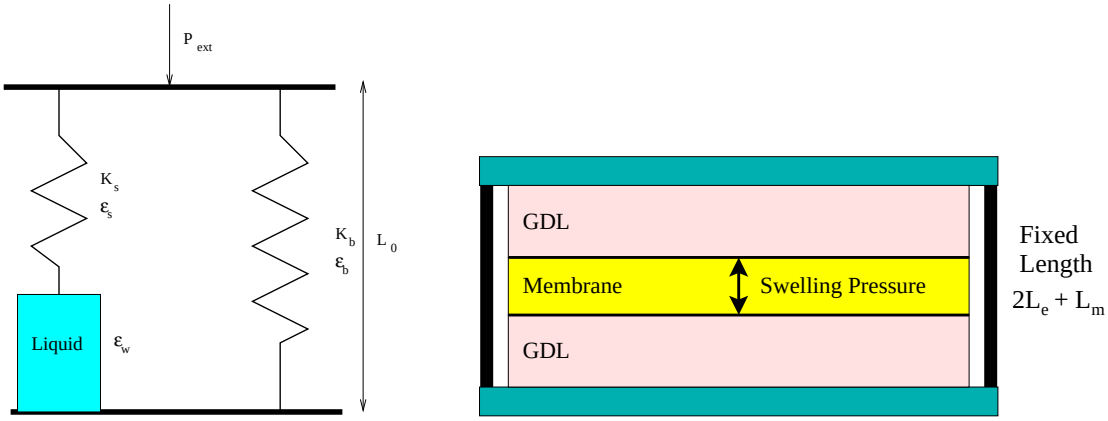

Figure 1 (Left) The force balance between the liquid water in the pores and the polymer backbone. The water is compressed by the side chains, carrying its compressional load in parallel with the backbone. (Right) The membrane and two gas diffusion layers are clamped between two plates with fixed distance $2L_e + L_m$. As the membrane swells it compresses the gas diffusion layers and generates clamping pressure.

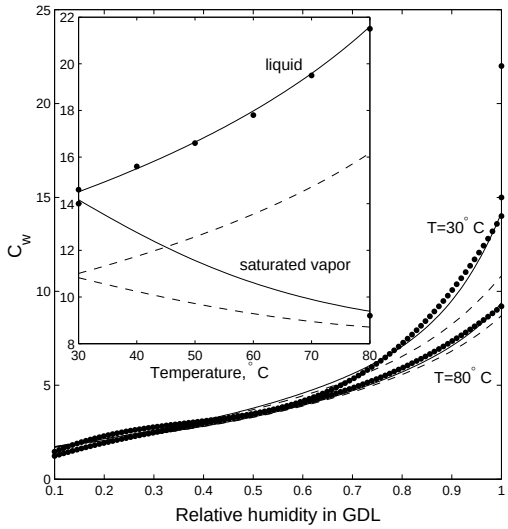

Figure 2 Nafion water uptake isotherms versus the relative humidity outside the membrane for $T = 30°C$ and $T = 80°C$ for unconstrained (solid) and a constrained (dotted) membrane with $K_{ext} = 10^9$ Pa. The dotted lines show the data by Hinatsu *et. al.* [4], for an unconstrained membrane at the two temperatures. The embedded figure shows the jump in equilibrium hydration isotherms of Nafion between saturated vapor- and liquid-equilibrated states as a function of temperature for both unconstrained (solid) and a constrained (dashed) membrane. The dots are data for an unconstrained membrane at the two temperatures.

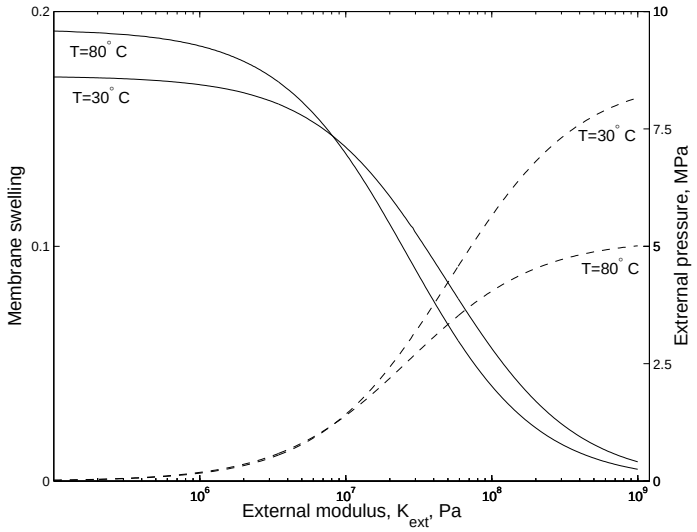

Figure 3 Membrane swelling versus the external constraint for two different temperatures at $I = 1.0\text{A/cm}^2$. The inset shows swelling pressure verses the elastic moduli of the GDL which confines the membrane at this current density.

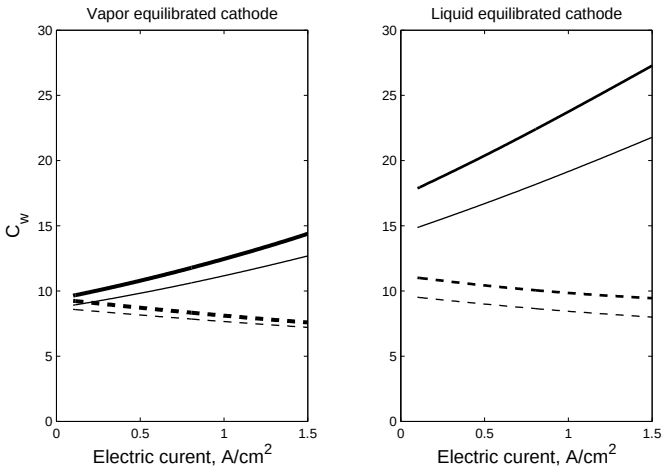

Figure 4: Water content at 80°C for the anode (dashed) and cathode (solid) ends of the membrane as a function of current density for both unconstrained, $K_e = 0$, (thick) and constrained, $K_e = 10^9$, (thin), conditions. (Left) Saturated vapor at both cathode and anode, (Right) liquid equilibrated cathode/vapor equilibrated anode.

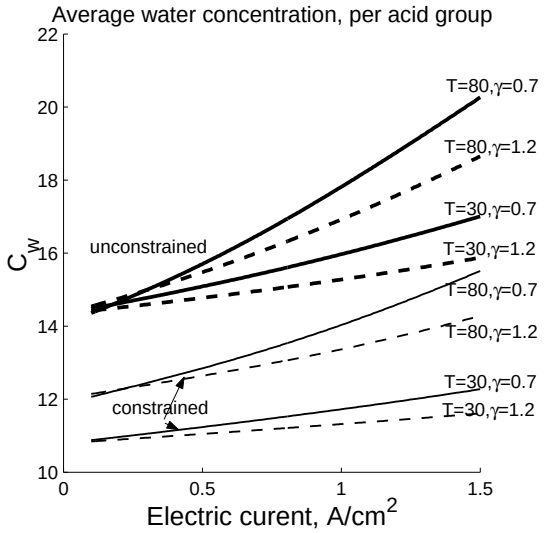

Figure 5: Average water content as a function of current density at 30° and 80°C, and for two values of the mass water transport parameter γ, for a liquid equilibrated cathode/saturated vapor equilibrated anode.

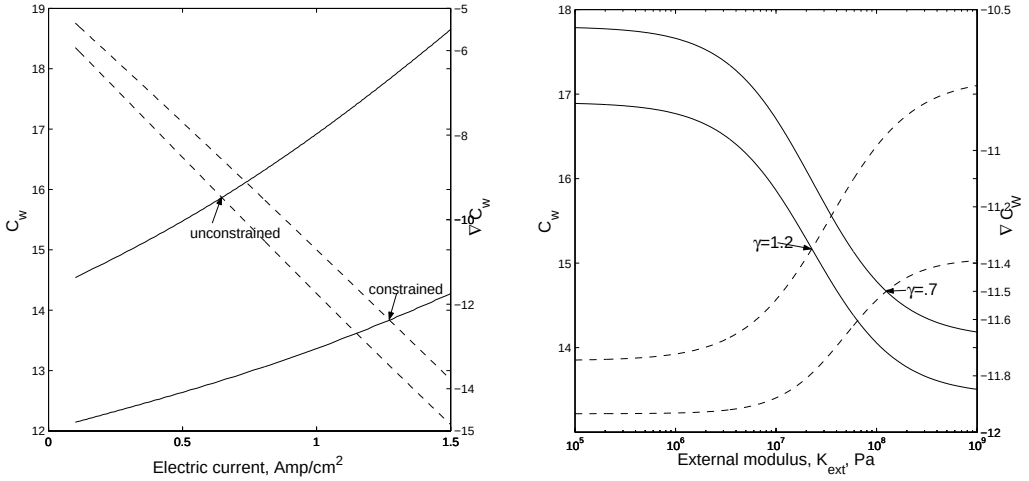

Figure 6: The average water content (solid) and the water content gradient (dashed) for (Left) both constrained $K_e = 10^9$ and unconstrained ($K_e = 0$) membranes, as a function of current density, and (Right) as a semi-log plot verses GDL elastic modulus at fixed current density of 1.0 A/cm^2.

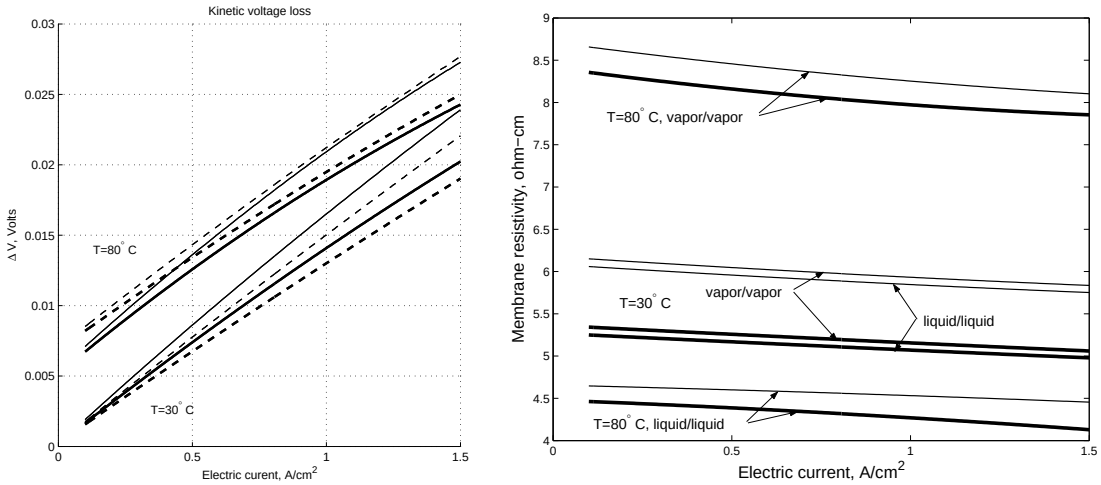

Figure 7: (left) Ohmic losses as a function of current density for a liquid equilibrated cathode and saturated vapor equilibrated anode, at 30 and 80°C. The four curves depict $\gamma = 0.7$ (solid), $\gamma = 1.2$ (dashed), unconstrained (thick), and constrained(thin) conditions. (Right) Membrane resistance versus the electric current for constrained (thin) and unconstrained (thick) membrane at two different temperatures and for homogenious boundary conditions (saturated vapor at both anode/cathode or liquid equilibration at both anode/cathode).

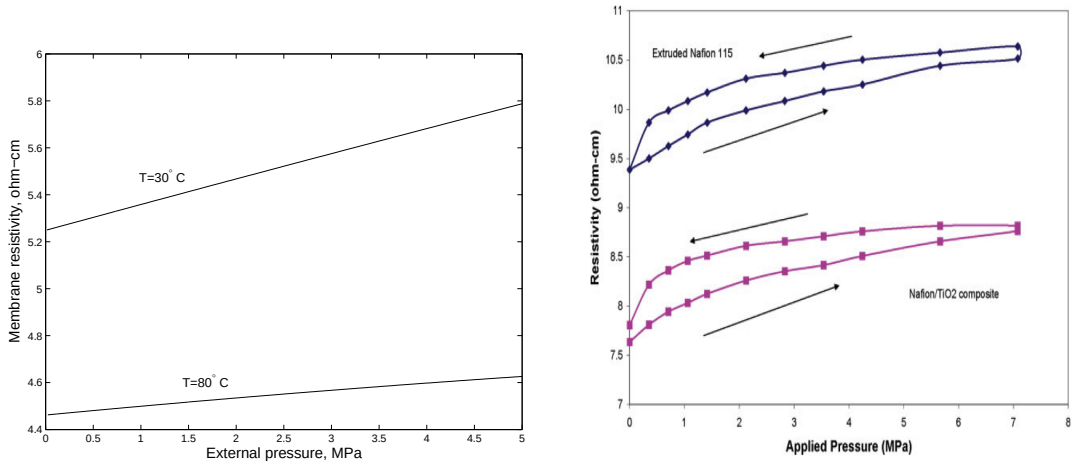

Figure 8: Membrane resistance versus the external load for liquid equilibration at both anode and cathode. (Left) Computational results at 0.1 A/cm^2 and (Right) experimental data from [13] for recast Nafion 115 at 30°C. In both the computational and experimental data the resistence increases by 10% under compression. The large membrane resistence for the experimental data could arise from contact resistence not present in the computations.

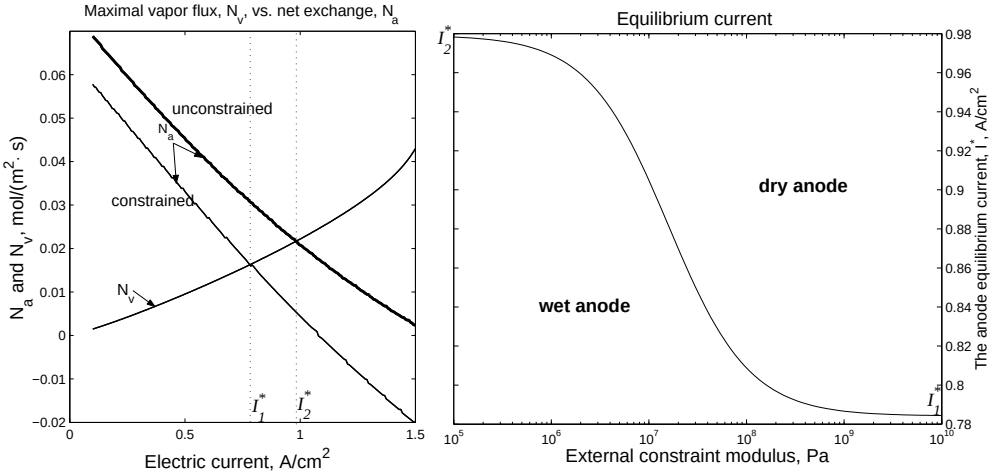

Figure 9: (Left) Maximal vapor flux, N_v and net exchange with the anode GDL, N_w^a as functions of current density for different conditions. (thick) $K_e = 0$, (thin) $K_e = 10^9$ Pa. The critical current densities at $K_e = 10^9$ Pa and $K_e = 0$ are marked by I_1^* and I_2^* respectively. (Right) A plot of the critical current densities as a function of the external modulus.